Overview of Results from the MST Reversed Field Pinch Experiment

J.S. Sarff[1], A.F. Almagri[1], J.K. Anderson[1], F. Auriemma[5], W.F. Bergerson[2], M. Borchardt[1], D.L. Brower[2], D. Carmody[1], S. Cappello[5], K. Caspary[1], B.E. Chapman[1], M. Cianciosa[10], D. Craig[8], V.I. Davydenko[6], P. Deichuli[6], D.R. Demers[3], D.J. Den Hartog[1], J. Duff[1], W.X. Ding[2], S. Eilerman[1], A. Falkowski[1], P. Fimognari[3], C.B. Forest[1], P. Franz[5], J.A. Goetz[1], J.D. Hanson[10], R.W. Harvey[9], D.J. Holly[1], P. Innocente[5], A.A. Ivanov[6], J.-H. Kim[1], J. King[1], J. Ko[1], J. Koliner[1], S. Kumar[1], J.D. Lee[1], L. Lin[2], D. Liu[1], R. Lorenzini[5], R. Magee[1], E. Martines[5], K.J. McCollam[1], M. McGarry[1], V.V. Mirnov[1], B. Momo[5], M.D. Nornberg[1], P.D. Nonn[1], S.P. Oliva[1], E. Parke[1], P. Piovesan[5], J. Polosatkin[6], M. Puiatti[5], J.A. Reusch[1], A. Seltzman[1], C.R. Sovinec[1], D. Spong[7], M. Spolaore[5], H. Stephens[1], D. Stone[1], N.V. Stupishin[6], D. Terranova[5], D. Theucks[1], M. Thomas[1], J. Titus[4], J. Triana[1], P.W. Terry[1], J. Waksman[1] and P. Zanca[5]

[1]University of Wisconsin, Madison, Wisconsin, and the Center for Magnetic Self-Organization in Laboratory and Astrophysical Plasmas
[2]The University of California at Los Angeles, Los Angeles, California
[3]Xantho Technologies, LLC, Madison, Wisconsin
[4]Florida A&M University, Tallahassee, Florida
[5]Consorzio RFX, Associazione EURATOM-ENEA sulla Fusione, Padova, Italy
[6]Budker Institute of Nuclear Physics, Novosibirsk, Russia
[7]The Oak Ridge National Laboratory, Oak Ridge, Tennessee
[8]Wheaton College, Wheaton, Illinois
[9]CompX, Del Mar, California
[10]Auburn University, Auburn, Alabama

Corresponding Author: jssarff@wisc.edu

Abstract:

An overview of results from the MST program on physics important for the advancement of the RFP as well as for improved understanding of toroidal magnetic confinement more generally is reported. Evidence for the classical confinement of ions in the RFP is provided by analysis of impurity ions and energetic ions created by 1 MW NBI. The first appearance of energetic particle modes by NBI in a RFP plasma is obtained. MST plasmas robustly access the quasi-single-helicity state that has commonalities to the stellarator and "snake" formation in tokamaks. The dominant mode grows to 8% of the axisymmetric field strength, while the remaining modes are reduced. Predictive capability for tearing mode behavior has been improved through nonlinear, 3D, resistive MHD computation using the measured resistivity profile and Lundquist number, which reproduces the sawtooth cycle dynamics. Experimental evidence and computational analysis indicates two-fluid effects, e.g., Hall physics and gyro-viscosity, are needed to understand the coupling of parallel momentum transport and current profile relaxation. Large Reynolds and Maxwell stresses, plus

separately measured kinetic stress, indicate an intricate momentum balance and possible origin for MST's intrinsic plasma rotation. Gyrokinetic analysis indicates that micro-tearing modes can be unstable at high beta, with a critical gradient for the electron temperature that is larger than for tokamak plasmas by roughly the aspect ratio.

1 Introduction

This overview of results from the MST reversed field pinch program summarizes physics important for the advancement of the RFP as well as for improved understanding of toroidal magnetic confinement in general. Topics include confinement physics, energetic particle effects, 3D helical equilibria, momentum transport, and magnetic self-organization physics. The MST is a large RFP device (R =1.5 m, a=0.5 m) that operates at medium plasma current ($I_p < 0.6$ MA). The RFP magnetic configuration offers several potential advantages for fusion as a result of the concentration of magnetic field within the plasma, including the possibility for fully-shielded normal magnets, a high particle density limit, and the possibility for Ohmic heating to burning plasma conditions. These features promote a fusion power vision for high power density and high reliability through the use of relatively simple technology. The RFP's large magnetic shear and weaker toroidal effects complement the physics regimes of tokamak and stellarator plasmas.

2 Classical Ion Confinement in the RFP

Evidence for the classical confinement of ions in the RFP is provided by (1) analysis of impurity ion transport in improved-confinement plasmas obtained with inductive current profile control and (2) energetic ion studies using 1 MW neutral beam injection. Each of these results is described below.

2.1 Impurity Ions

The RFP is unlike the tokamak and stellarator configurations in that the gradient in $|\mathbf{B}|$ is almost normal to magnetic surfaces, everywhere on a surface. The magnetic connection length is also shorter, since $B_p \sim B_t$. The drift of particle guiding centers off a magnetic surface is therefore small, e.g., the banana orbit width for trapped particles is less than their gyroradius. For perpendicular transport, the lower limit to transport in the RFP is thus classical, not neoclassical, despite the fraction of trapped particles being about the same as for a tokamak configuration with the same aspect ratio. Fluctuation-induced transport in the RFP has typically been dominated by parallel losses in the stochastic magnetic field associated with MHD tearing instabilities. In recent years, inductive pulsed parallel current drive (PPCD) has been developed to create RFP plasmas with improved tearing stability, yielding a ten-fold increase in the global energy and particle confinement times.[1] With PPCD, the test-particle diffusivity for ions in a stochastic magnetic field is reduced below the classical transport level.

Measurements of impurity ions obtained by charge-exchange recombination spectroscopy (CHERS) in PPCD plasmas have allowed a comparison of the experimental ion confinement with classical transport expectations.[2, 3] The radial profile of the fully-stripped carbon density is measured to be hollow, as shown in Fig. 1, revealing outward particle convection and low particle transport. Modeling of the diffusion of impurity ions for classical transport agrees well with the measured carbon profile evolution, and temperature screening explains the hollow profile, expected when the temperature profile is more peaked than the density profile. The modeling is time dependent and includes collisional coupling between the dominant ion species in MST plasmas. The comparison in Fig. 1 is made about 10-15 ms following the application of PPCD. The hollow profile is predicted to appear within 10 ms, due to the anti-pinching effect of the temperature screening mechanism. It is noteworthy that a tokamak plasma with the same collisionallity as for MST plasmas would be expected to have a peaked impurity ion density profile. The observed hollow profile is thus a clear signature of classical transport in this case.

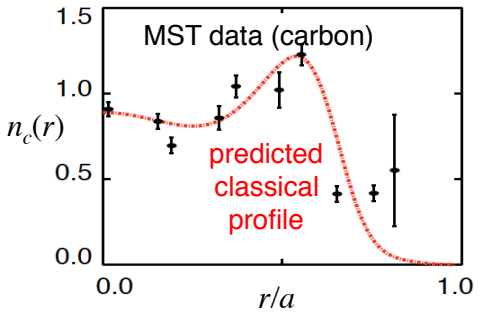

FIG. 1: Radial profile of the carbon density measured using CHERS, compared with modeling for classical transport in the RFP.

2.2 Energetic Ions from Neutral Beam Injection

Classical confinement is also observed for energetic ions created by 1 MW, 25 keV neutral beam injection (NBI).[2] The injector installed on MST is the first tangential NBI experiment performed in an RFP plasma [4]. (There is only one other high-power NBI experiment performed previously in an RFP, on the TPE-RX experiment [5].) The hydrogen beam is doped with 3% deuterium to observe the slowing-down of the fast ion population via the decay of the d-d fusion neutron flux after sharp NBI turn-off, like the "beam-blip" technique used in other experiments. The measured characteristic neutron decay time can be separated as $\tau_{n-exp}^{-1} = \tau_{n-classical}^{-1} + \tau_{fi}^{-1}$, where $\tau_{n-classical}$ is the classical slowing-down time dominated by electron collisions, and τ_{fi} represents all other losses, including those associated with charge-exchange and turbulence. Over a wide range of MST plasma conditions, the fast ion confinement is close to classical, i.e., $\tau_{n-exp} \approx \tau_{n-classical}$, as shown in Fig. 2. In all cases, the fast-ion confinement time exceeds the thermal ion con-

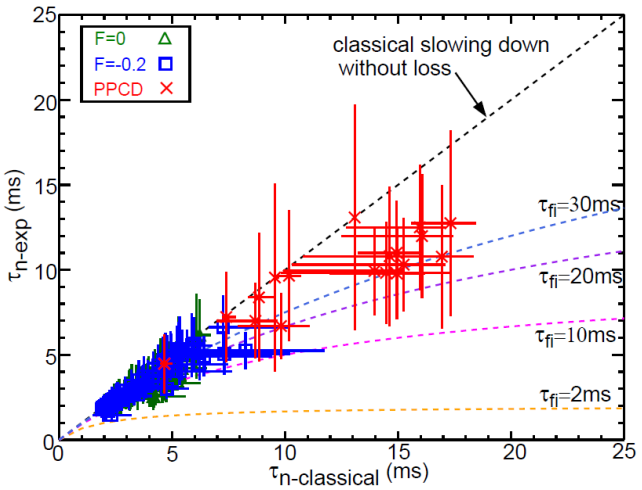

FIG. 2: The measured neutron decay time versus the classical slowing down time for a variety of MST plasma conditions. PPCD plasmas are hotter, with longer slowing down times.

finement time, τ_p = 1-10 ms. This is true even in standard RFP plasmas with large tearing instabilities that yield a stochastic magnetic field.

The energetic ions have super-Alfvenic speed and a strong density gradient in the core, stimulating the first appearance of fast-particle-driven modes by NBI in a RFP plasma.[2, 6] The tangential NBI geometry creates a fast ion population localized to $r/a \lesssim 0.1$, with $v_{||} \gg v_\perp$ and $v_{fi}/v_A > 1$. Using the NUBEAM module in TRANSP, the predicted fast ion density is 25% of the local electron density, implying the local fast-ion beta in the core is $\beta_{fi} > 15\%$. (The fast ion density is yet to be directly measured.) Several new fast-ion-driven modes are observed, one illustrated in Fig. 3, which shows a magnetic spectrogram for toroidal mode number n=5 measured by a toroidal array of magnetic sensors at the plasma surface. The poloidal mode number is dominantly $m = 1$. This mode and two others with $n = 4$ and $n = 1$ are bursty in character, appearing only with NBI. (The bright mode with $f \sim 20$ kHz is an $m = 1$ tearing mode resonant in the core.) The n=5 mode exhibits a scaling with the beam energy, with little dependence on the background plasma Alfven speed. This mode is energetic-particle-like. The n=4 mode exhibits scaling with the Alfven velocity (magnetic field, density and ion mass varied), with weak dependence on the beam energy. While this is Alfvenic-like, both the n=4 and n=5 modes have frequencies that are smaller than expected for toroidal Alfven eigenmodes that have been analyzed using AE3D and STELLGAP.[6] The n=4 mode is therefore speculated to be a resonant branch of the kinetic ballooning mode. MST's complement of advanced diagnostics is rapidly characterizing these modes, e.g., using FIR interferometry, scattering, and polarimetry that yield the radial profiles of the fluctuating density and magnetic field.

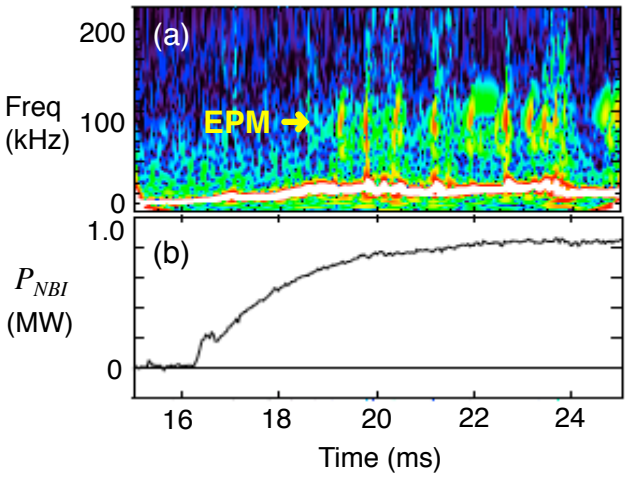

FIG. 3: (a) Magnetic spectrogram for n=5 and (b) the neutral beam injection power.

3 Quasi-single-helicity Configuration

The quasi-single-helicity (QSH) state that forms spontaneously in RFP plasmas [7, 8] has commonalities to the stellarator and "snake" formation in tokamak plasmas. The QSH state is characterized by the growth of one toroidal mode in the tearing mode spectrum, while the other modes are reduced. A helical structure within the plasma therefore becomes apparent. The strongest form of QSH appeared first in RFX-mod when plasma operations pushed to high current $I_p > 1$ MA and plasmas with a single helical magnetic axis formed, called the single-helical-axis (SHAx) configuration.[9] The SHAx configuration has now been formed in MST as well, notably with $I_p \sim 0.5$ MA, lower than the threshold for their appearance in RFX-mod. This apparent difference in current threshold, and the scaling for the QSH regime in

general, may be better unified if there is a dependence on Lundquist number. The MST case is produced at lower density and higher temperature, and thus similar Lundquist number despite lower plasma current (i.e., lower B). The SHAx state in MST is accessible most robustly with shallow toroidal field reversal, which is also the typical operating regime for RFX-mod. This could indicate that limiting the appearance of m=0 modes and commensurate nonlinear coupling to m=1 modes may be key to long-lasting QSH periods. The dominant helical mode in MST has toroidal mode number n=5 and grows as large as 8% of the axisymmetric field. The secondary m=1 modes are reduced, implying reduced magnetic stochasticity. Measurements of the global energy confinement show an improvement of $\sim 50\%$ with SHAx. If elements of current profile control are included, e.g., allowing the plasma current to slowly decay, the improvement in confinement is as large as three-fold in SHAx plasmas.

MST's substantial diagnostic set for core measurements is well suited to advancing 3D equilibrium reconstruction methods. This work is proceeding using the V3FIT code, which is based on VMEC.[10] An preliminary example of a V3FIT reconstruction is shown in Fig. 4 that employs only magnetic diagnostics outside the plasma. Diagnostics such as FIR interferometry and polarimetry and motional Stark effect have not yet been included as constraints in the reconstructions. A new 2-color soft x-ray tomography system is near completion and will provide high time resolution reconstructions of the electron temperature in a poloidal plane. Previous work using FIR interferometry/polarimetry indicates that these diagnostics will be extremely valuable reconstruction constraints.[11]

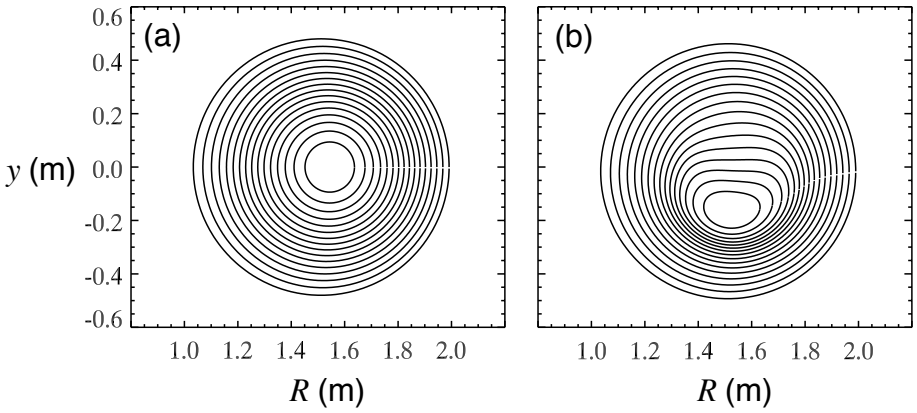

FIG. 4: Flux plots in a poloidal plane from preliminary magnetic reconstructions using V3FIT for (a) the standard RFP case and (b) single-helical-axis (SHAx) case with $B_{n=5}(a)/B(a) = 8\%$. The phase of the n=5 perturbation in (b) is selected to emphasize the helical nature by showing a downward shift of the helical magnetic axis.

4 Predicting the Sawtooth Cycle and Stochastic Transport

The ability to perform computational modeling with parameters approaching those in experiments has improved through advances in computational resources. Nonlinear resistive MHD computation (DEBS code) with Lundquist number and resistivity profile matching MST standard RFP plasmas has been completed to investigate the tearing mode relaxation process.[12, 13] Such a comparison is valuable for validation efforts. The maximum Lundquist number for these calculations is $S = \tau_R/\tau_A = \mu_0 a V_A/\eta = 4 \times 10^6$, and the magnetic Prandtl number, $P_m = \mu_0 \nu/\eta$, is allowed to dynamically range from $\sim$ 250 between crashes to $\sim$ 3000 during the crash for numerical stability. The Prandtl number based on Braginskii coefficients for experimental parameters is $P_m \sim 1$, although the role of turbulent viscosity is unclear and would tend to increase the effective P_m. The calculation is also force-free, whereas the experimental plasmas have $\beta \approx 5\%$.

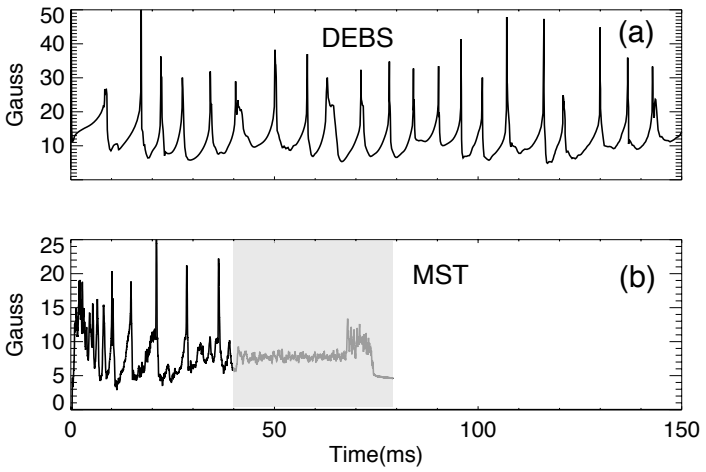

FIG. 5: The rms amplitude of the m=1 magnetic fluctuations measured at r=a in (a) the DEBS simulation and (b) MST experiment.

A comparison of the rms magnetic fluctuation amplitude for m=1 modes is shown in Fig. 5. The characteristic sawtooth relaxation cycle is evident in the fluctuation amplitude, with the simulation closely resembling the experimental behavior. Other effects are also in good agreement but not shown here, such as the modification of the plasma current profile at the sawtooth crash. Note that the simulation is time-advanced for an effective pulse length 150 ms, longer than the flattop portion of a single MST discharge. The greyed out portion of the MST waveform corresponds to the current ramp-down phase when the toroidal electric field is turned off, and hence the drive for current profile peaking and tearing instability is reduced. While the temporal dynamics of the sawtooth cycle are clearly similar, the fluctuation amplitude in the simulation is systematically about two times larger than measured in MST. The resolution of this difference may lie in effects beyond resistive MHD. For example, recent linear analysis of non-reduced MHD with the Hall term and gyro-viscosity shows that two-fluid effects tend to provide stability for the tearing modes.[17] This could possibly explain lower amplitudes in

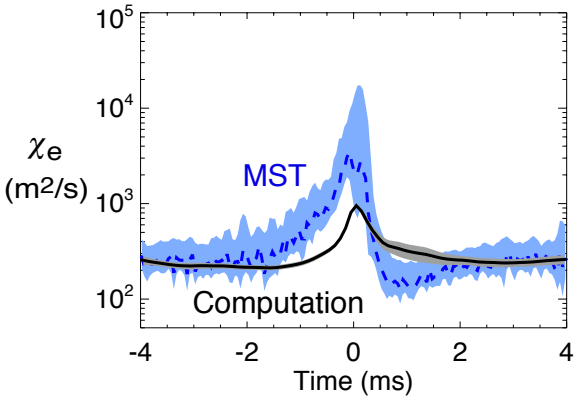

FIG. 6: The electron heat conductivity during a sawtooth cycle (crash at $t = 0$) compared with the stochastic transport prediction.

nonlinear saturation.

The DEBS simulations also provide a more refined representation of the magnetic field for evaluation and comparison of energy transport in a stochastic magnetic field.[12, 13] The magnetic diffusivity, D_m, is evaluated directly from field line tracing using the DEBS mode spectrum, adjusted to match the experimental mode amplitudes. This is necessary since the predicted stochastic transport, $\chi_{st} = v_{th} D_m$, is expected to scale as $D_m \sim (\tilde{B}/B)^2$. Since the mode amplitudes are dynamic over the sawtooth cycle, this provides a stringent test of this scaling. The electron heat diffusivity was measured for the sawtooth cycle taking advantage of high rep rate lasers in MST's Thomson scattering diagnostic. A comparison of the measured heat diffusivity, χ_e, with $\chi_{e,st} = f_c v_{th,e} D_m$, is shown in Fig. 6, where $f_c \sim 0.5$ is the fraction of circulating electrons. The equilibrium field has a magnetic mirror associated with the toroidal geometry which leads to a trapped particle fraction comparable to that in a tokamak configuration of the same aspect ratio. This comparison is made in the mid-radius region of the plasma where the density of m=1 resonant surfaces is high and the magnetic stochasticity is robust. The $\sim$ 2X reduction in $\chi_{e,st}$ from particle trapping yields better agreement with measured χ_e.

5 Plasma Flow and Momentum Transport

MST plasmas exhibit spontaneous plasma rotation, despite being ohmically heated. The flows are both perpendicular and parallel to the magnetic field, with the poloidal and toroidal components being similar in magnitude. This flow appears early on and dynamically varies during the sawtooth cycle. For example, the parallel flow profile peaks between sawtooth crash events, and then flattens during the crash. The sawtooth cycle for the flow in the core region is shown in Fig. 7. Previous MST measurements using probes in the edge and Faraday rotation in the core identified large Reynolds and Maxwell stresses associated with fluctuations at the tearing mode scale.[14, 15] The force densities from these stresses are enormous compared to the plasma inertia, but they tend to oppose each other. The spatially-averaged correlation $\langle \tilde{\mathbf{J}} \times \tilde{\mathbf{B}} \rangle_{||}$ appears in the parallel ohm's law as a Hall emf and in the parallel momentum balance as the Maxwell stress, so a coupling of electron and ion momentum processes during the relaxation process is exposed.

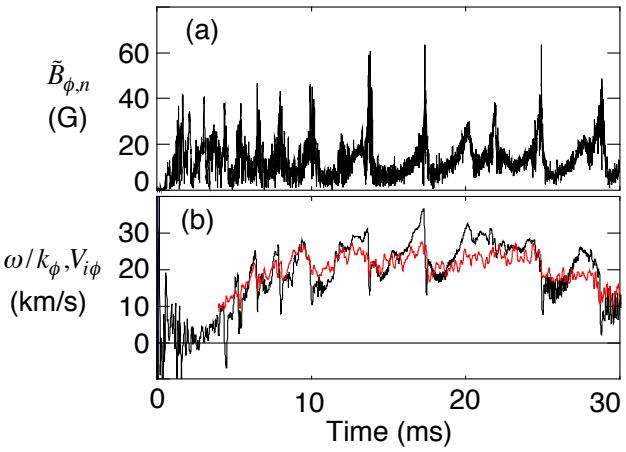

FIG. 7: (a) The n=6 magnetic fluctuation amplitude and (b) n=6 toroidal phase velocity (black) and plasma flow (red).

New work in this area includes (1) computational modeling using a non-reduced MHD model with two-fluid effects and (2) the experimental identification of a new turbulent stress associated with the correlation of plasma pressure and magnetic field fluctuations. The computational modeling is done using the NIMROD code with the inclusion of the Hall term in ohm's

law and gyro-viscosity in the momentum-density evolution.[16, 17] Similar to experimental observations, the force densities from the Reynolds and Maxwell stresses that appear in nonlinear multi-mode calculations tend to oppose each other. (The Hall term also produces a mean-field emf, $\langle \tilde{\mathbf{J}} \times \tilde{\mathbf{B}} \rangle_{||}/en_e$, that is comparable in magnitude to $\langle \tilde{\mathbf{V}} \times \tilde{\mathbf{B}} \rangle_{||}$.) Thus a theoretical context to understand the coupled relaxation processes for current and momentum is emerging.

A new, separate fluctuation-induced stress has been measured that is associated with the correlation $\langle \tilde{p}_{||} \tilde{B}_r \rangle$.[18] This term is the heart of a "kinetic stress" for parallel flow stemming from $\nabla \cdot \mathbf{P}$ in momentum balance. For measurement purposes, the pressure fluctuation is assumed separable as $\tilde{p}_{||} = T_{||}\tilde{n} + n\tilde{T}_{||}$, and an FIR inteferometer-polarimeter is used to measure directly only the term $T_i \langle \tilde{n} \tilde{B}_r \rangle$, using a Rutherford scattering diagnostic for the ion temperature measurement, T_i. While the magnitude of the kinetic stress is small compared to the Reynolds and Maxwell stresses described above, its force density is nevertheless comparable to the plasma inertia. It is also better resolved, in particular its magnitude between sawtooth crash relaxation events. The radial profile of the kinetic stress is directed to increase the parallel flow between sawtooth crash events, so it is important in the context of the spontaneous rotation of MST plasmas. The spontaneous rotation and momentum transport in magnetic relaxation thus involves an intricate balance of several fluctuation-induced stresses.

6 Non-collisional Ion Heating

Non-collisional ion heating is very powerful during the sawtooth crash phase, with the ion temperature reaching $T_i \sim$ 2-3 keV. Several features of the heating process have been uncovered recently, including a majority ion mass dependence [19] and anisotropy [12, 20], $T_\perp \geqslant T_{||}$ (measured in impurity ions using CHERS). Measurements of an apparent excess in d-d neutron flux implies that the ion distribution must not be Maxwellian. New compact neutral particle analyzer (CNPA) measurements observe this energetic tail with a power-law energy dependence that is created spontaneously during the strong magnetic reconnection during the sawtooth crash.[20] This is shown in Fig. 8. Similar measurements in astrophysical plasmas with tails having a power-law distribution are common. The CNPA energy limit is 5 keV, but if the power-law is extrapolated to energy $\sim$ 20 keV, the implied neutron flux is consistent with measurements. A second advanced NPA with higher energy range $\sim$ 30 keV has recently been installed on MST, motivated by the 1 MW NBI experiments. Evidence for the energetic tail appears in the ANPA's initial data.

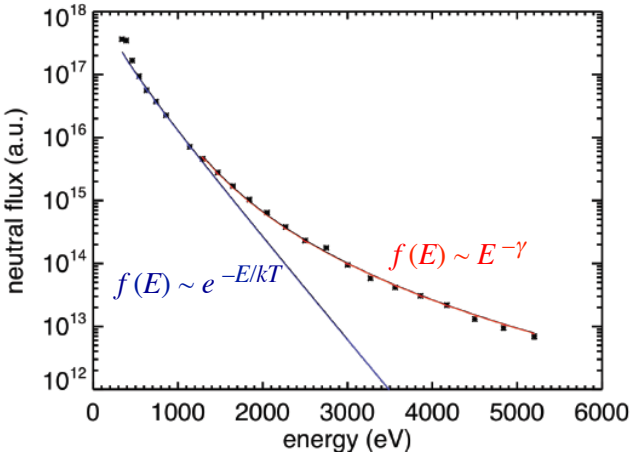

FIG. 8: Neutral (deuterium) flux energy spectrum measured by the CNPA.

7 Micro-turbulence in the RFP

Microturbulence from drift-wave-like instabilities might be important in the RFP when magnetic fluctuations are reduced. New gyrokinetic analysis indicates that micro-tearing modes can be unstable at high beta, with a critical gradient for the electron temperature that is larger than for tokamak plasmas by roughly the aspect ratio.[21] Ion-temperature-gradient (ITG) turbulence is unstable in MST-like discharges for $a/L_T >$ 3-4 at zero-β.[22] As β is increased, the ITG growth rate is reduced until a different instability becomes dominant in the growth rate spectrum for $\beta > 5\%$, as shown in Fig. 9. Finite beta stabilization of ITG occurs as in the tokamak, through coupling to shear Alfven waves, and is controlled by the parameter $d\beta/dr$. The critical β for stabilization is higher in the RFP than for the tokamak by a factor proportional to the aspect ratio, a consequence of the smaller connection length in the RFP equilibrium. The mode that dominates instability above the critical β has a structure along the magnetic field line with odd parity in the electrostatic potential and even parity in the vector potential. This, and the mode frequency, identify the mode as micro-tearing. The mode has a temperature gradient threshold that is very close to that of ITG, with the growth rate rising more steeply than for the tokamak equilibrium as a/L_T increases above 3-4. This steep rise of growth with temperature gradient will produce profile stiffness in the temperature gradient. The micro-tearing growth rate is largest at moderate collisionality. Surprisingly, the growth rate remains significant even when the collisionality is small. The growth rate is sensitive to the curvature drift. The curvature drift frequency, which is neglected in tokamak micro-tearing theories, is larger in the RFP by a factor R/r. The larger value arises from the large poloidal field and its curvature scale length of radial displacement r. Variation of growth rate with curvature drift frequency, which is artificially modified in the code, behaves in a similar way to the magnetic-curvature drift-tearing instability [23]. Growth rates behave similarly across a wide range of collisionality, from the semi collisional regime to the collisionless limit, indicating that there is a collisionless branch of the instability not previously described. The MST experiment includes diagnostics such as fast Thomson scattering, FIR scattering, and a heavy ion beam probe that have the capability to identify micro-turbulence at these scales.

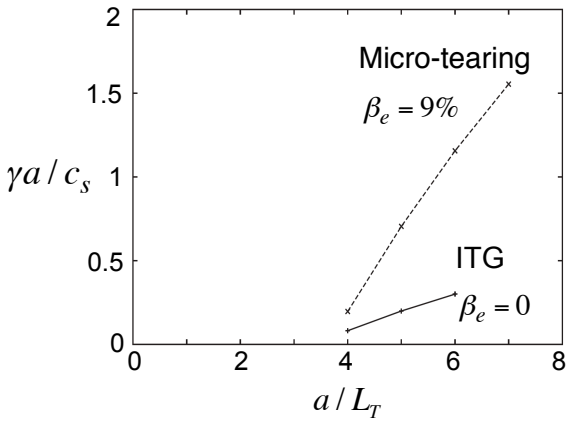

FIG. 9: Linear growth rates of the most unstable modes versus the normalized temperature gradient scale length for β =0 and 9%. The growth rate is normalized to c_s/a, where c_s is the sound speed and a is the minor radius.

Acknowledgements

Work supported by U.S. Department of Energy and National Science Foundation

References

[1] Chapman, B.E., J.W. Ahn, A.F. Almagri, J.K. Anderson, F. Bonomo, D.L. Brower, D.R. Burke, et al., Nuclear Fusion 49, 104020 (2010).

[2] J.K. Anderson et al, EX/P3-16 this conference.

[3] Kumar, S. T. A., D. J. Den Hartog, K. J. Caspary, R. M. Magee, V. V. Mirnov, B. E. Chapman, D. Craig, G. Fiksel, and J. S. Sarff, Physical Review Letters 108, 125006 (2012)

[4] Anderson, J.K. et al., Fusion Sci. and Tech. 59, 27 (2011).

[5] H. Sakakita, S. Kiyama, Y. Hirano, Y. Yagi, H. Koguchi, T. Shimada, Y. Sato, and K. Hayase, in 30th EPS Conference on Contr. Fusion and Plasma Phys. (2003).

[6] Koliner, J. J., C. B. Forest, J. S. Sarff, J. K. Anderson, D. Liu, M. D. Nornberg, J. Waksman, et al, Physical Review Letters 109115003 (2012).

[7] B.E. Chapman et al., EX/P6-01 this conference.

[8] Martin, P, L Marrelli, G Spizzo, P Franz, P Piovesan, I Predebon, T Bolzonella, et al., Nuclear Fusion 43, 1855 (2003)

[9] Lorenzini, R., E. Martines, P. Piovesan, D. Terranova, P. Zanca, M. Zuin, A. Alfier, et al., Nature Physics 5, 570 (2009).

[10] Hanson, James D., Steven P. Hirshman, Stephen F. Knowlton, Lang L. Lao, Edward A. Lazarus, and John M. Shields, Nuclear Fusion 49, 075031 (2009).

[11] Bergerson, W. F., F. Auriemma, B. E. Chapman, W. X. Ding, P. Zanca, D. L. Brower, P. Innocente, et al., Physical Review Letters 107, 255001 (2011).

[12] D.J. Den Hartog et al, EX/P3-17 this conference.

[13] Reusch, J. A., J. K. Anderson, D. J. Den Hartog, F. Ebrahimi, D. D. Schnack, H. D. Stephens, and C. B. Forest, Physical Review Letters 107, 155002 (2011).

[14] Ding, W. X., D. L. Brower, D. Craig, B. H. Deng, G. Fiksel, V. Mirnov, S. C. Prager, J. S. Sarff, and V. Svidzinski, Physical Review Letters 93, 045002 (2004).

[15] Kuritsyn, A., G. Fiksel, A. F Almagri, D. L Brower, W. X Ding, M. C Miller, V. V Mirnov, S. C Prager, and J. S Sarff, Physics of Plasmas 16, 055903 (2009).

[16] C.R. Sovinec et al., TH/P3-08 this conference.

[17] King, J. R., C. R. Sovinec, and V. V. Mirnov, Physics of Plasmas 19, 055905 (2012).

[18] W. Ding et al., EX/P3-08 this conference.

[19] Fiksel, G., A. F. Almagri, B. E. Chapman, V. V. Mirnov, Y. Ren, J. S. Sarff, and P. W. Terry, Physical Review Letters 103, 145002 (2009).

[20] Magee, R. M., D. J. Den Hartog, S. T. A. Kumar, A. F. Almagri, B. E. Chapman, G. Fiksel, V. V. Mirnov, E. D. Mezonlin, and J. B. Titus, Physical Review Letters 107, 065005 (2011)

[21] D. Carmody et al., TH/P2-10 this conference.

[22] Tangri, Varun, P. W. Terry, and R. E. Waltz, Physics of Plasmas 18, 052310 (2011).

[23] Finn, J., and Drake, J.F., Phys. Fluids 29 (1986) 3672.